Journal of Energy Chemistry 65 (2022) 637–645

Contents lists available at ScienceDirect

Journal of Energy Chemistry

journal homepage: www.elsevier.com/locate/jechem

http://www.journals.elsevier.com/journal-of-energy-chemistry/

Correlating the electronic structure of perovskite $La_{1-x}Sr_xCoO_3$ with activity for the oxygen evolution reaction: The critical role of Co 3d hole state

Zechao Shen [a], Mei Qu [a], Jueli Shi [a], Freddy E. Oropeza [b], Victor A. de la Peña O'Shea [b], Giulio Gorni [c], C.M. Tian [d], Jan P. Hofmann [d], Jun Cheng [a], Jun Li [a], Kelvin H.L. Zhang [a,*]

[a] State Key Laboratory of Physical Chemistry of Solid Surfaces, College of Chemistry and Chemical Engineering, Xiamen University, Xiamen 361005, Fujian, China
[b] Photoactivated Processes Unit, IMDEA Energy Institute, Parque Tecnológico de Móstoles, Avda. Ramón de la Sagra 3, 28935 Móstoles, Madrid, Spain
[c] CELLS-ALBA Synchrotron, Carrer de la Llum 2-26, 08290 Cerdanyola del Vallès, Spain
[d] Surface Science Laboratory, Department of Materials and Earth Sciences, Technical University of Darmstadt Otto-Berndt-Strasse 3, 64287 Darmstadt, Germany

ARTICLE INFO

Article history:
Received 17 May 2021
Revised 22 June 2021
Accepted 23 June 2021
Available online 16 July 2021

Keywords:
Perovskite oxide
Oxygen evolution
Cobalt
Electronic structure

ABSTRACT

Perovskite $LaCoO_3$ is being increasingly explored as an effective low-cost electrocatalyst for the oxygen evolution reaction (OER). Sr doping in $LaCoO_3$ ($La_{1-x}Sr_xCoO_3$) has been found to substantially increase its catalytic activity. In this work, we report a detailed study on the evolution of the electronic structure of $La_{1-x}Sr_xCoO_3$ with $0 \leq x \leq 1$ and its correlation with electrocatalytic activity for the OER. A combination of X-ray photoemission spectroscopy (XPS) and X-ray absorption spectroscopy (XAS) was used to unravel the electronic density of states (DOS) near the Fermi level (E_F), which provide insights into the key electronic structure features for the enhanced OER catalytic activity. Detailed analysis on the Co *L*-edge XAS suggest that $LaCoO_3$ has a low spin state with $t_{2g}^6 e_g^0$ configuration at room temperature. This implies that the high OER catalytic activity of $LaCoO_3$ should not be rationalized by the occupancy of $e_g = 1$ descriptor. Substituting Sr^{2+} for La^{3+} in $LaCoO_3$ induces Co^{4+} oxidation states and effectively dopes hole states into the top of valence band. A semiconductor-to-metal transition is observed for $x \geq 0.2$, due to the hole-induced electronic DOS at the E_F and increased hybridization between Co 3d and O 2p. Such an electronic modulation enhances the surface adsorption of the *OH intermediate and reduces the energy barrier for interfacial charge transfer, thus improving the OER catalytic activity in $La_{1-x}Sr_xCoO_3$. In addition, we found that the $La_{1-x}Sr_xCoO_3$ surface undergoes amorphization after certain period of OER measurement, leading to a partial deactivation of the electrocatalyst. High Sr doping levels accelerated the amorphization process.

1. Introduction

Electrochemical water splitting is widely seen as a promising means of storing renewable energy for global sustainable energy future [1–3]. The key to enable this approach is the development of low-cost and efficient electrocatalysts to accelerate the water splitting reactions [4–6]. However, this task still represents a grand scientific challenge because the overall efficiency is mostly limited by the sluggish and energy-demanding water oxidation, *i.e.*, oxygen evolution reaction (OER), which involves multiple-step reaction mechanism with the transfer of multiple electrons and protons [7,8]. This has stimulated world-wide upsurge in the search for earth-abundant transition metal oxides (TMO) as efficient electrocatalysts viable for large-scale application [9,10].

Perovskite TMOs are attractive electrocatalysts for promoting the OER because of its tunable electronic structure and high activity [11]. Perovskite has a general ABO_3 structure, with rare-earth and/or alkaline large cations at the A site and transition metals (TM) at the B site. Since the TM has significant contribution to the electronic states near the Fermi level (E_F) of the oxide, the physicochemical properties are strongly susceptible to the type and chemistry (e.g., oxidation state, coordination and spin state) of the TM in perovskite structure. The chemistry of the TM in the B site can be widely modulated by substitution at A site, *e.g.*, La^{3+} for Sr^{2+}, leading to fascinating properties such as metal–insula tor-transition, colossal magnetoresistance, and catalytic perfor-

* Corresponding author.
E-mail address: kelvinzhang@xmu.edu.cn (K.H.L. Zhang).

https://doi.org/10.1016/j.jechem.2021.06.032
2095-4956/

mance [11–14]. The electronic structure near the E_F dictates the binding strength with reaction intermediates and the energy barrier for charge transfer across the interface, and therefore substantially impact the catalytic activity [15,16]. Understanding the relation between the electronic structure and the OER catalytic activity is crucial for devising high-performance electrocatalytic materials. Many studies have attempted to use various electronic properties of TMOs as descriptors of the OER catalytic activity. Suntivich *et al.* proposed the occupancy of the e_g orbital of TM cations as a descriptor because the e_g orbitals have strong interaction with oxygen adsorbates due to its preferable vertical orbital overlap with O 2p. They found a volcano type correlation between the OER catalytic activity and the e_g occupancy in the TM of a series of perovskite oxides, with optimum at an occupancy of nearly one electron. Higher e_g filling results in too weak binding of the reaction intermediates, and a lower e_g filling results in too strong binding, leading in both cases to detriments in the OER performance [17]. Other proposed descriptors include the TM d band center, TM 3d − O 2p hybridization degree and the position of O 2p band center relative to the E_F [18–20].

However, there are deviations from the above-mentioned descriptors. For example, $LaMnO_3$ with e_g occupancy of one electron has low OER activity [12]. Furthermore, phase transformation and surface reconstruction during the OER process complicate the use of these descriptors to predict OER activity [21,22]. Multiple descriptors are necessary to explain the OER activity, which require a thorough understanding of the material electronic properties. $LaCoO_3$ is an attractive material under extensive investigation, because of its high catalytic activity for the OER [23–25]. Besides, $LaCoO_3$ has been widely used in many related applications such as photoelectrochemical water splitting, catalytic oxidation of VOCs, and the oxygen reduction reaction [26–29]. The high OER activity of $LaCoO_3$ was ascribed to the intermediate spin (IS) state of Co^{3+} (*i.e.* $t_{2g}^5e_g^1$) [17]. Based on this, many following works reported that the spin state of Co^{3+} in $LaCoO_3$ was low spin (LS) with $t_{2g}^6e_g^0$ configuration and it could be tuned to intermediate spin with $t_{2g}^5e_g^1$ *via* controlling crystal orientation, surface modifying or doping for higher OER activity [30–32].

However, it is interesting to re-visit the correlation of the electronic structure of $LaCoO_3$ with its OER catalytic activity. $LaCoO_3$ is a semiconductor with a bandgap of ~ 0.6 eV. The Co^{3+} cation is coordinated by six oxygen ions in a CoO_6 octahedron [33]. As illustrated in Fig. 1, the $3d^6$ electrons in Co^{3+} could be in different spin states, such as the LS with a $t_{2g}^6e_g^0$ configuration, IS with $t_{2g}^5e_g^1$ at room temperature or high spin (HS) with $t_{2g}^4e_g^2$ at temperatures above ~ 500 K [34]. The replacement of La^{3+} with Sr^{2+} in $LaCoO_3$ was reported to induce Co^{4+} oxidation state for regulating the electronic properties [35,36]. Depending on the initial spin state of Co^{3+} cation, the introduction of Co^{4+} would reduce the occupancy of e_g or t_{2g} orbitals. In the case of IS with a $t_{2g}^5e_g^1$ configuration, Sr^{2+} doping would lead to the loss of electrons in e_g orbital, which induces a $t_{2g}^5e_g^0$ configuration for Co^{4+}, and thus would decrease the OER catalytic activity according to the e_g electron descriptor [17]. However, it has been demonstrated that differently doped $La_{1-x}Sr_xCoO_3$ exhibit much higher OER activity than $LaCoO_3$ [35,36]. Consequently, an understanding on how electronic structure changes in $LaCoO_3$ introduced by Sr doping influence the OER requires a more though investigation.

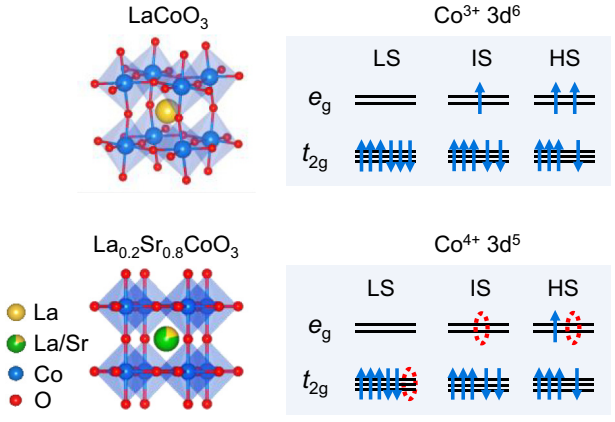

Fig 1. Representative crystal structures of $LaCoO_3$ and $La_{0.2}Sr_{0.8}CoO_3$ with different spin configuration of Co^{3+} and Co^{4+}, respectively.

Herein, we report a detailed study on the influence of Sr doping on the electronic structure of $La_{1-x}Sr_xCoO_3$ and the associated OER catalytic activities. We synthesized polycrystalline $La_{1-x}Sr_xCoO_3$ powders with × = 0, 0.2, 0.4, 0.6, 0.8 and 1 (denoted as LSCO-*x*) for investigating their electronic structure and OER catalytic activity. A combination of X-ray photoemission spectroscopy (XPS) and X-ray absorption spectroscopy (XAS) was used to measure the occupied and unoccupied DOS at the E_F to provide insights into the electronic structure relevant for the OER. Detailed analysis on Co *L*-edge XAS shows that the Co^{3+} in $LaCoO_3$ is at LS state with $t_{2g}^6e_g^0$ configuration. Replacing La^{3+} with Sr^{2+} in $LaCoO_3$ induces Co^{4+} oxidation state and the formation of a hole (empty) state with t_{2g} character at the top of VB. With the Sr level of × ≥ 0.2, DOS is observed at the E_F, indicating a semiconductor-to-metal transition. By quantitative analysis of O *K*-edge XAS spectra, we also found a considerable increase in Co 3d-O 2p hybridization at higher Sr doping levels. The increase in the Co 3d-O 2p hybridization and higher Co^{4+} oxidation states enhance the surface adsorption of *OH intermediate and reduce the energy barrier for interfacial charge transfer, thus improving the OER activity in $La_{1-x}Sr_xCoO_3$.

2. Experimental

2.1. Material synthesis

The $La_{1-x}Sr_xCoO_3$ (x = 0, 0.2, 0.4, 0.6, 0.8 and 1) polycrystalline powders were synthesized using a modified sol–gel method. Stoichiometric amounts of $La(NO_3)_3$ (Alfa, 99.9%), $Sr(NO_3)_2$ (Alfa, 99.9%), and $Co(NO_3)_3{\cdot}6H_2O$ (Alfa, 99.9%) were mixed in 20 mL Milli-Q deionized water (18 MΩ cm). Citric acid was added as chelating agent in sequence in a 2:1 molar ratio to the total metal cations. 1.2 mL of ethylene glycol was also added to the solution. After evaporation of solvent, the resultant gel was heated in furnace at 400 °C for 4 hours in air to form a brown precursor. The precursor was grounded and calcined at 1000 °C for 12 hours in 1 atm O_2 gas.

2.2. Material characterizations

The samples were characterized by XRD (Rigaku, Japan) operating at 40 kV and 40 mA with Cu K_α radiation (λ = 0.15418 nm). Rietveld refinement was used to determine the lattice parameters by GSAS software and EXPGUI interface. The morphology and microstructures of the samples were investigated using scanning electron microscopy (SEM) and JEOL 2100 transmission electron microscopy (TEM). The samples were dispersed on carbon tape for SEM measurement. For TEM, the samples were dispersed in a solution of water/isopropanol with volume ratio of 3:1 by ultrasonication for 1 hour to form a homogeneous ink and then dropped on Cu grid. The Brunauer-Emmett-Teller (BET) specific surface area was obtained by the isothermal N_2 adsorption and desorption at 77 K (ASAP 2020, Micromeritics, USA). The contents of oxygen vacancies in LSCO-*x* were measured by iodometric titrations.

20 mg LSCO-*x* powders was added in 3 mL of de-oxygenated KI solution. 1 M HCl solution was added to dissolve the perovskite oxides. Then, the solution was titrated to a faint golden color with $Na_2S_2O_3$ which was standardized by KIO_3. Starch indicator was then added to mark the endpoint. The conductivity test was conducted using Keithley 2401 Source Meter at room temperature with four-probe method. For the conductivity test, powders of LSCO-*x* were pressed under 12 MPa pressure, then sintered at 1000 °C for 24 hours in 1 atm O_2 gas, producing pellets of LSCO-*x* with density of ~ 5.4 g cm^{-3}.

For XPS and XAS measurements, the powders were pressed into pellets. XPS was measured using a monochromatic Al $K_{\alpha 1}$ X-ray ($h\nu$ = 1486.6 eV) source at normal emission (electron take-off angle = 90° relative to the surface plane) with a SPECS PHOIBOS 150 electron energy analyzer. The binding energy was calibrated using an Au foil. The total energy resolution was about 0.50 eV. XAS measurements were performed at the Soft X-ray Spectroscopy Beamline of the Australian Synchrotron. The XAS measurements at the O *K*-edge and Co *L*-edge were performed in total electron yield (TEY) using linearly polarized X-rays at room temperature.

2.3. Electrochemical measurements

The electrochemical measurements were performed on a three-electrode system controlled by an electrochemical workstation (CHI 760E) with glassy carbon rotating disk electrode configuration (RDE, Pine Research Instrumentation). For OER tests, an Hg/HgO (1 M KOH) electrode was used as the reference electrode, and a graphite rod was used as the counter electrode. All tests were performed in O_2-saturated 1 M KOH (Adamas, 99.999%) electrolyte (pH = 14) using a catalyst-modified glassy carbon (GC) working electrode (0.196 cm^2). To prepare the working electrodes, 10 μL catalyst ink were prepared by dispersing 5 mg LSCO-*x* powder in 1 mL of 750 μL H_2O and 250 μL isopropanol and 50 μL Nafion solution (5 wt%). The ink was ultrasonicated for 30 minutes and then drop-casted on the GC surface with a catalyst loading of 0.25 mg cm^{-2}_{geo}. Cyclic voltammetry tests were performed at a scan rate of 0.1 V s^{-1} and a rotation of 1600 rpm from 0.2 V to 0.8 V vs. Hg/HgO. LSV data were collected at 10 mV s^{-1}. The Tafel slope was extracted from LSV data. The electrochemical impedance spectroscopy (EIS) measurements were performed at 1.63 V (vs. RHE) under an alternating voltage of 5 mV from 100 kHz to 0.1 Hz. All potential values were calibrated to reversible hydrogen electrode (RHE) using the following equation: $E(\text{RHE}) = 0.0591 \times \text{pH} + E_{\text{Hg/HgO}} + E_{\text{applied}}$. For electrical double-layer capacitance measurements, cyclic voltammetry was conducted in the potential window of 0.1 V centered at open circuit potential with different scan rates (20 mV s^{-1} to 100 mV s^{-1}).

3. Results and discussion

3.1. Crystal structure and morphology

The LSCO-*x* powders were synthesized *via* a sol–gel method. Fig. 2(a) shows the powder XRD patterns. The patterns show that LCO and LSCO-0.2 crystallize in a rhombohedral perovskite structure featured by the double-peak structure at ~ 33° 2θ (Fig. 2(b)). With higher Sr doping level in LSCO-0.4, 0.6 and 0.8, the double-peak feature turns into one peak, suggesting phase transformation from the rhombohedral to a cubic lattice [37,38]. Additionally, it was difficult to synthesize perovskite $SrCoO_3$, a brownmillerite structure $SrCoO_{2.5}$ is commonly formed (Fig. S1) [39,40]. Therefore, in the present work, we do not include the study for LSCO-1. The crystal structures of LSCO-*x* are further verified by Rietveld refinement analysis of the XRD patterns (Fig. S2). Fig. 2(c) summarizes the evolution of lattice parameters derived from XRD refinement.

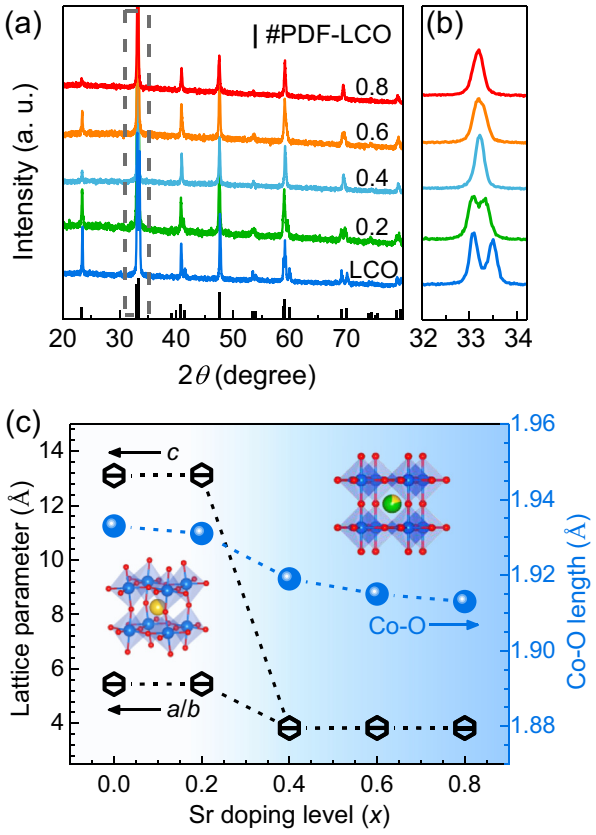

Fig 2. (a) Powder XRD patterns of LSCO-*x* (LCO, *x* = 0.2, 0.4, 0.6, 0.8); (b) zoom-in XRD patterns at the 2θ region of 32°–34°; (c) evolution of lattice parameters and Co – O bond length determined from Rietveld refined XRD as *a* function of *x*.

LCO exhibits a rhombohedral structure with lattice parameters $a = b = 5.441$ Å and $c = 13.102$ Å. With Sr doping, the lattice parameters of *a*, *b* and *c* shrink from LSCO-0.2 to LSCO-0.4, accompanying with the transition from rhombohedral to cubic phase. Meanwhile, the Co – O bond length decreases from 1.933 Å for LCO to 1.913 Å for LSCO-0.8. The reduction of lattice parameters and Co – O bond length from the refined XRD patterns is ascribed to the higher oxidation states of Co^{4+} induced by Sr^{2+}. The substitution of Sr^{2+} for La^{3+} introduces Co^{4+} together with the creation of oxygen vacancies for charge compensation. The contents of oxygen vacancies in LSCO-*x* series were determined by iodometric titration. As shown in Table S1, the oxygen contents for $\times$ < 0.4 are nearly stoichiometric (2.99). With higher Sr content, oxygen vacancies start to form, *i.e.*, the oxygen content is 2.93 for LSCO-0.6 and 2.90 for LSCO-0.8. As can be seen, the amount of oxygen vacancies created in LSCO-*x* is relatively small.

Analysis of the nitrogen adsorption–desorption isotherms with BET method shows that the LSCO-*x* series have similar surface areas in the range of 2.0 to 2.5 m^2 g^{-1} (Fig. S3). SEM was also performed to study the powder morphologies and size (Fig. S4). All LSCO-*x* powders possess similar morphology, specific surface area and distribution of particle size. Based on the little variation of surface area and morphology within the LSCO-*x* series, we exclude the influence of these parameter on the OER activities discussed below [41–43].

3.2. Evolution of electronic structure

XPS and XAS were performed to investigate the evolution of electronic structure of LSCO-*x* as function of *x*. $LaCoO_3$ is a p-type

semiconductor with a bandgap of 0.6 eV. Sr introduces hole states in LSCO-*x*. Fig. 3(a, c) shows the La 4d, Sr 3d and O 1 s XPS core level spectra. The binding energies (BEs) of La 4d, Sr 3d and O 1 s concurrently shift towards lower values upon increasing Sr^{2+} contents [44]. Because all photoemission spectra are referenced to the E_F as zero, the shift of BEs to lower values indicates shift of the E_F towards the VB, which is characteristic of doping of p-type carriers in semiconductors [45,46]. On the other hand, the Co 2p core-levels shift towards higher BEs with increasing Sr level, as shown in Fig. 4 (a). All spectra in the Co 2p region show a similar spin–orbit splitting of ~15.2 eV between the $2p_{3/2}$ and $2p_{1/2}$ components. The Co $2p_{3/2}$ peak position for LCO is located at a BE of 780 eV, in agreement with the Co^{3+} oxidation state, whereas the Co $2p_{3/2}$ peak position is located at 780.4 eV for LSCO-0.8, suggestive of the higher Co^{4+} oxidation states.

The Co *L*-edge XAS was also measured to examine the change in Co oxidation states, as it probes the excitation of Co 2p core electrons into unoccupied Co 3d orbital [47]. As shown in Fig. 4(b), the Co *L*-edge splits into L_3 and L_2 due to spin–orbit splitting. For LCO, the Co L_3 and L_2 locate at ~ 778 and ~ 792 eV, respectively. The lineshape of the multiplets in Co *L*-edge XAS conveys information on spin configuration of Co, as it reflects the Coulomb and exchange interactions between the photon-excited Co 2p hole and unpaired Co 3d electrons [48]. Here, the lineshape of the Co *L*-edge spectrum of LCO is very similar to the experimental and calculated Co *L*-edge spectra of LCO with LS configuration and that of $LiCoO_2$ with Co LS configuration, suggesting the synthesized LCO has a LS with $t_{2g}^6e_g^0$ configuration at room temperature [49,50]. With Sr doping, the characteristic peaks of Co^{4+} at ~ 777 eV and ~ 794 eV arise [51,52]. An energy shift of up to ~ 0.3 eV was also observed in the Co *L*-edge spectra upon doping LCO with Sr. The shifts of $L_{2,3}$ edges to higher photon energy further confirms the induced Co^{4+} *via* Sr doping [53].

A comprehensive understanding of the occupied and unoccupied states near the E_F of electrocatalysts, including the hybridization of TM 3d with O 2p is of paramount importance for elucidating the relation of electronic structure with catalytic activity. We used VB XPS and O *K*-edge XAS to further examine the occupied and unoccupied DOS near the E_F for LSCO-*x*. Fig. 5(a) shows the measured VB photoemission spectra. For LCO, peak A near ~ 1 eV is attributed to the t_{2g}^6 electron in LS Co^{3+}, and peaks B and C in the region of 3 ~ 6 eV are attributed to the dominant O 2p states hybridized with Co 3d [44]. We can see that the spectral intensity of peak A becomes weaker with increasing Sr content, suggesting the hole states are created in the t_{2g} orbital. Besides, it can be observed in Fig. 5(a, b) that the occupied state in the VB is shifted towards the E_F. Certain DOS across the E_F is also observed for $x \geq 0.2$ as displayed in Fig. 5(b), indicating a semiconductor-to metal transition in the LSCO-*x* induced by the increasing hole state at the top of the VB upon Sr doping. As shown in Fig. 5(d), the electrical conductivities of the LSCO-*x* pellets are significantly increased from $1x10^{-3}$ S cm^{-1} for LCO to 40 S cm^{-1} for LSCO-0.8.

The O *K*-edge XAS probes the excitation of the O 1 s electron to unoccupied states of O 2p states hybridized with Co 3d above the E_F. O *K*-edge XAS spectra for LSCO-*x* are shown in Fig. 5. For LCO, there is a single peak located at ~ 528.5 eV (marked as peak "D"). Peak D can be ascribed to the unoccupied state associated with the empty e_g orbital (see Fig. 1) [54]. As La^{3+} is replaced by Sr^{2+}, a new hole state (marked as "E") appears and its spectral intensity systematically increases with the Sr doping level. Meanwhile, there is negligible change in the spectral intensity of peak "D". The newly created hole state should be associated with the emptied t_{2g} orbi-

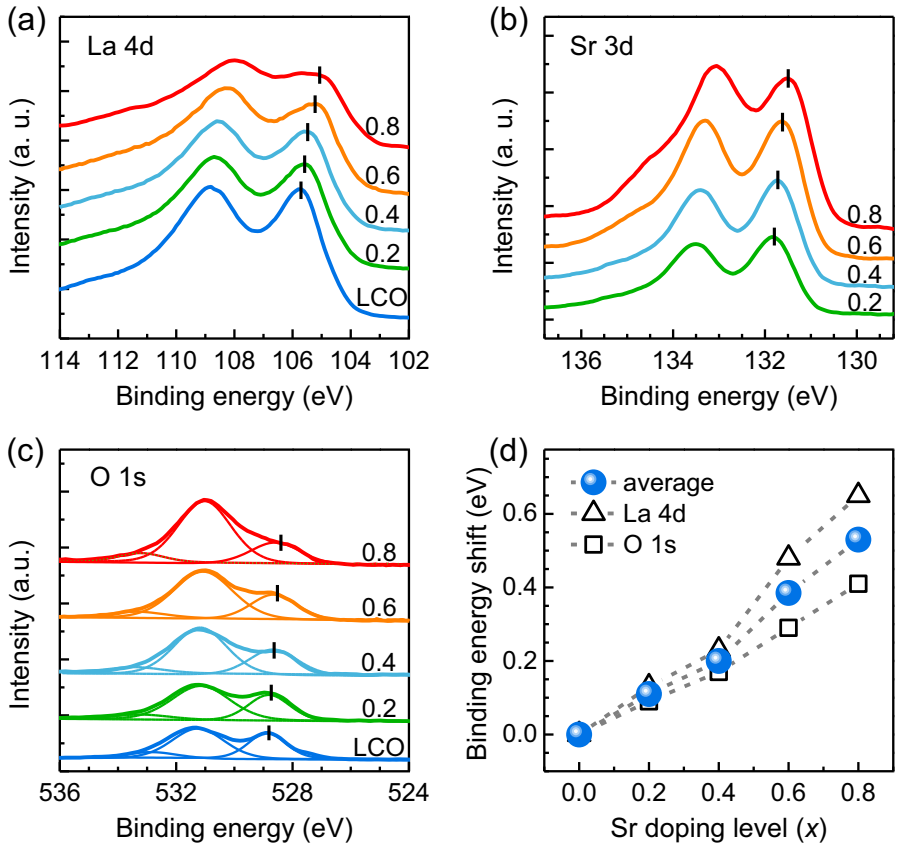

Fig 3. (a) La 4d, (b) Sr 3d and (c) O 1 s core level XPS spectra; (d) the binding energy shift of La 4d, O 1 s and the averaged shift relative to LCO as a function of Sr doping level *x*.

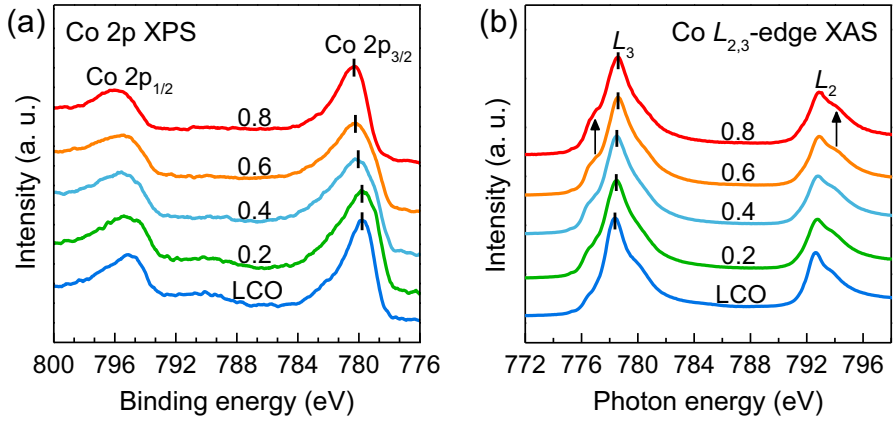

Fig 4. (a) Co 2p core level XPS spectra; (b) Co $L_{2,3}$-edge XAS.

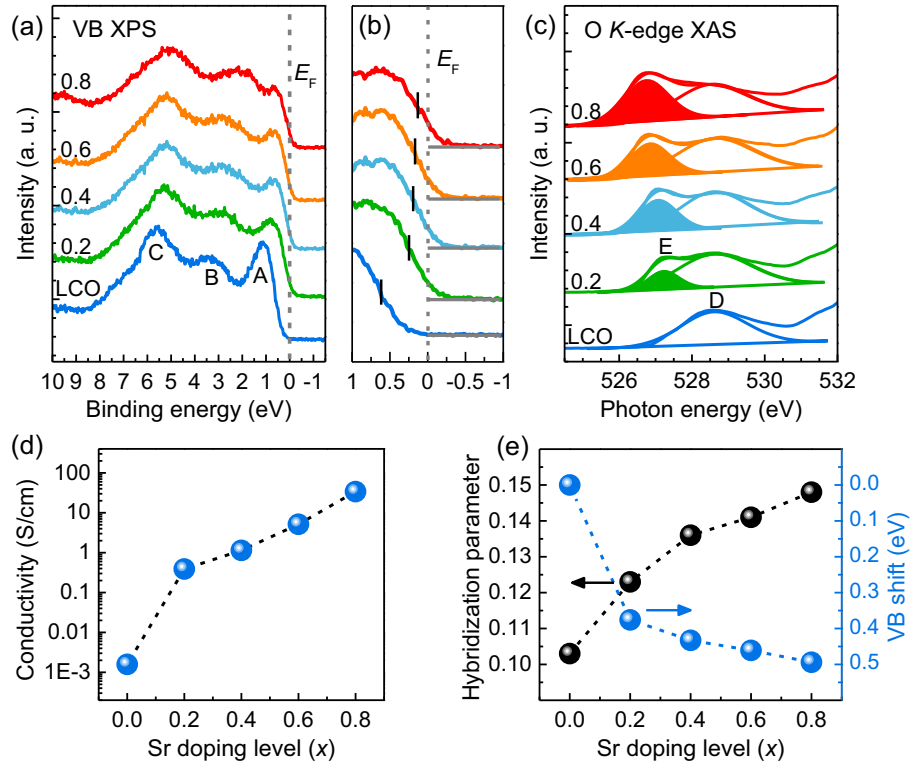

Fig 5. (a) VB XPS spectra of LSCO-*x*; (b) zoom-in VB XPS spectra around the E_F region; (c) O *K*-edge XAS; (d) the change of electrical conductivity as a function of *x*; (e) the shift of the midpoint of the edge of VB as marked in Fig. 5(b), and the estimated degree of Co 3d-O 2p hybridization as a function of *x*, deduced from O *K*-edge XAS.

tals. This further proves that the oxidation of Co^{3+} with $t_{2g}^6e_g^0$ is converted into Co^{4+} with $t_{2g}^5e_g^0$ *via* Sr doping, which is in accordance with Co *L*-edge XAS and VB XPS results. We also quantitatively determined the Co 3d-O 2p hybridization using O *K*-edge XAS based on the method developed by Suntivich *et al.* [55]. Details of the method are described in Fig. S5 and Table S2. Fig. 5(e) shows the degree of hybridization as a function of Sr content, showing the hybridization of Co 3d-O 2p becomes stronger with higher Sr doping level.

Fig. 6 shows the schematic illustration of the electronic structure near the E_F for LCO and LSCO-0.8 derived from VB XPS and O *K*-edge XAS. LCO is a semiconductor with bandgap of 0.6 eV. It has a LS state with occupied t_{2g}^6 forming the top of VB and unoccupied e_g^0 forming the bottom of CB. When Sr^{2+} replaces La^{3+}, a hole state is created with t_{2g} character. The E_F moves into the VB, leading to occupied DOS across the E_F and thus metallic state in LSCO-0.8. In addition, the hybridization of Co 3d-O 2p is also substantially increased, because of an increased overlap between O 2p and Co 3d resulting from the higher valence Co^{4+}.

3.3. Electrocatalytic OER performance

The OER activities of LSCO were characterized in 1 M KOH using a rotating disk electrode. The current densities were normalized to the BET surface area. Fig. 7(a) shows the normalized linear sweep voltammetry (LSV) curves after three cycles of CV measurement for all samples. In Fig. 7(b), Tafel slopes derived from LSV curves show substantial decrease from 131 mV dec^{-1} for LCO to 85 mV dec^{-1} for LSCO-0.8. Fig. 7(c) shows the electrochemical impedance spectroscopy (EIS) conducted at 1.63 V (vs. RHE). The inset shows

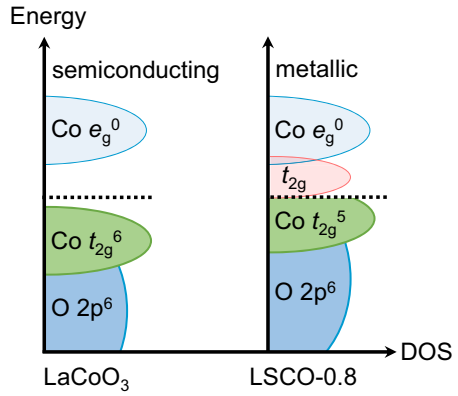

Fig 6. Schematic illustration of the electronic structure of LCO (semiconducting) and LSCO-0.8 (metallic), derived from VB XPS and O *K*-edge XAS.

the fitted equivalent electrical circuit. The fitted charge transfer resistance decreases from 2700 Ω for LCO to 220 Ω for LSCO-0.8, as summarized in Table S3. The reduction in charge transfer resistance at the interface indicates the enhanced charge transfer kinetics.

To investigate the stability of LSCO-*x* during OER process, 30 cycles of CV for LCO and LSCO-0.8 were measured and the current variation followed as a function of number of cycles, as shown in Fig. 8(a) and S6. The current density at 1.63 V vs. RHE for both LCO and LSCO-0.8 shows negligible change in the first 5 cycles, and gradually decreases between the 5th and 15th CV measurements. High resolution TEM was used to examine the surfaces of pristine LCO and LSCO-0.8 and samples after 5 and 30 cycles of CV measurements, as shown in Fig. 8(b and c). The results show that both LCO and LSCO-0.8 retain the pristine crystalline surface for the first 5 CV cycles, which correlates well with the negligible activity decay at the beginning of the stability study. After 30 cycles of CV, their surface reconstructs with the occurrence of an amorphous layer. It can be seen that the extent of surface reconstruction for LSCO-0.8 is larger than that for LCO after 30 CV cycles. The surface instability of LSCO-0.8 is ascribed to the strong hybridization of O 2p with Co 3d, where the lattice oxygen may be activated to participate in the OER [19,20]. Since the LSV curves and EIS shown in Fig. 7 were acquired after three cycles of CV measurements, the OER activities still reflect the properties of crystalline LSCO-*x*.

3.4. Correlation of OER activities with electronic structure

Insights into the electronic structure of LSCO reveal that Sr substitution in $LaCoO_3$ induces Co^{4+} oxidation state and a hole state with predominant t_{2g} character. With the Sr level × ≥ 0.2, the LSCO features a metallic electronic state, which provides the materials with high electrical conductivity. Quantitative analysis on O *K*-edge XAS spectra also indicates a considerable increase in the Co 3d-O 2p hybridization at higher Sr doping level. The electronic density of states at the E_F determines the binding strength between catalysts and the reaction intermediates. The metallic state for samples with the × ≥ 0.2 introduces occupied and unoccupied states at the E_F (see Fig. 6), giving rise to facile reduction and oxidation of the Co cations for catalyzing the OER reaction. The conventional adsorbate evolution OER mechanism in alkaline electrolyte includes four elementary steps with different adsorbed intermediates in sequence of *OH, *O, *OOH and $*O_2$ [56]. According to the OER mechanistic study using DFT calculations by Lee *et al.*, the adsorption of *OH is the rate-determining-step (RDS) for OER activity on LCO, because of the weak interaction between *OH and electronic states associated with Co^{3+} [57]. It has been reported that high valent TM cations have a strong tendency to interact with *OH [58–61]. Therefore, the stronger interaction of Co^{4+} with oxygen intermediates such as *OH would be vital for OER. Fig. 9(a) shows the O 1 s core level photoemission spectra, which can be fitted into three components originating from lattice oxygen ($O_{lattice}$) at ~ 528.5 eV, hydroxides (OH) at ~ 531 eV and carbonates (C – O) at ~ 533.5 eV [62–64]. It can be seen that the surface OH content substantially increases with × (Table S4), which can be associated with an enhanced adsorption of *OH. Fig. 9(b) plots the OER activities as a function of the surface OH content for different Sr doping level. It can be clearly depicted that the OER activities correlate well with the surface OH content.

To further confirm the stronger adsorption of OH^- during the electrochemical process, comparative CV measurements within the non-Faradaic potential region were conducted in 1 M KOH and 1 M K_2SO_4 (Figs. S7, S8 and Tables S5 and S6) [65]. The charging current of the non-Faradaic CV (i_{charge}) is equal to the product of the scan rate (v) and the double-layer capacitance (C_{dl}), as given by the equation below [66,67]:

$$i_{charge} = vC_{dl}$$

Fig. 9(c) shows the results of the C_{dl} for LSCO-*x*. The C_{dl} in KOH and K_2SO_4 increases with Sr doping, indicating that the modified electronic structure in LSCO-*x* improves the surface adsorption for oxygen species, in accordance with increasing C_{dl} values

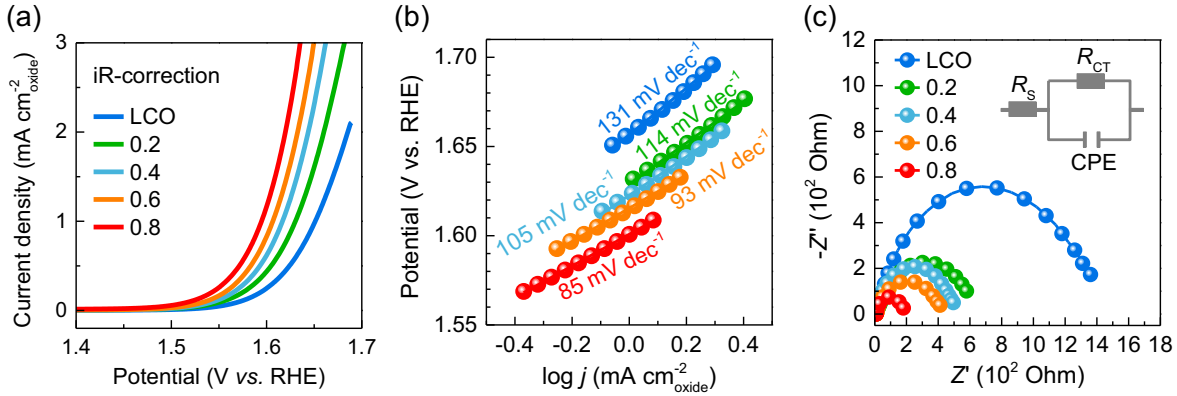

Fig 7. (a) OER LSV polarization curves with iR-correction, and (b) the corresponding Tafel slopes of LSCO-*x* series; (c) Nyquist plot at 1.63 V (vs. RHE), inset shows the equivalent circuit diagram.

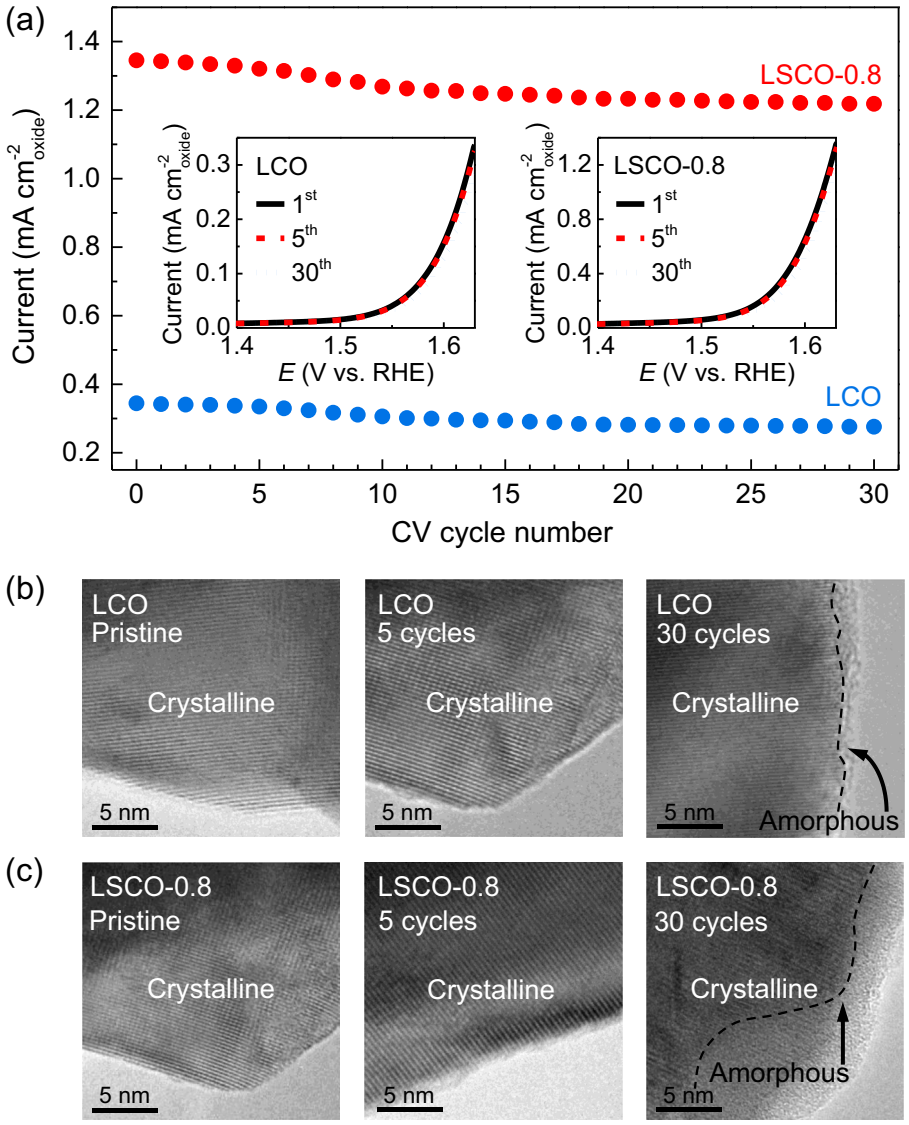

Fig 8. (a) 30 cycles of CV measurements and the recorded current at 1.63 V (vs. RHE) for each CV cycle, inset shows the polarization curve extracted from the 1st, 5th and 30th cycle of CV, respectively; (b and c), high-resolution TEM images of LCO and LSCO-0.8 after different cycles of CV measurements, including pristine, 5 cycles, 30 cycles.

derived from EIS measurement (Table S3). Besides, the larger C_{dl} values in KOH indicates that LSCO-*x* have stronger interaction with hydroxides. The interplay between surface Co and *OH is illustrated in Fig. 9(d). For LCO, the fully occupied Co^{3+} 3d t_{2g}^6 has significant electronic repulsion to O 2p. Sr doping in LCO gives rise to hole states with t_{2g} character. The hole states at Co^{4+} 3d t_{2g}^5 weaken the electronic repulsion to O 2p, thus enhancing the orbital overlap and the hybridization of Co 3d-O 2p, so that the Co^{4+}–OH has stronger binding strength than Co^{3+}–OH. Rossmeisl and Nørskov *et. al* studied the OER mechanism *via* DFT calculations and the results showed that the RDS of OER was adsorption of *OH when the binding strength was too weak, whereas for the strong binding with intermediates, the RDS would be the formation of *OOH species [7]. In LSCO system, the hole state in Co^{4+} 3d results in enhanced hybridization between Co 3d and O 2p, which leads to strong attraction of Co^{4+} 3d orbitals for the O 2p electron. As a result, the interaction between O 2p and protons becomes weaker in Co^{4+}–OH, which promotes the deprotonation of *OH to form *O [68]. In this aspect, the surface *O can bind OH^- ions to form *OOH, thus the strong binding of Co^{4+} with *OH may change the RDS for OER according to the study by Rossmeisl and Nørskov *et. al.*

The charge transfer barrier associated with the position of the CB can be used to rationalize the overall trend of OER activity of the first-row transition metal (Mn, Fe, Co, Ni) perovskite. Fig. 10 shows the schematic of energy band position for $LaMnO_3$, $LaFeO_3$, LCO ($LaCoO_3$) and $LaNiO_3$, and the O_2/OH^- redox energy level [16,61,69]. The energy difference between the CB and O_2/OH^- redox energy level is defined as the energy barrier for charge transfer associated with OER. For $LaCoO_3$ and $LaNiO_3$, their band positions of CB are relatively low and close to the E_F thus the energetic barrier for charge transfer from the O_2/OH^- redox level to unoccupied CB is smaller. Since optimized charger transfer energy promotes the OER kinetics, $LaCoO_3$ and $LaNiO_3$ shows superior OER activity than $LaMnO_3$ and $LaFeO_3$ [70]. These results indicate that optimizing the charge transfer energy from oxygen intermediates to metal 3d hole in CB is the key to enhance OER

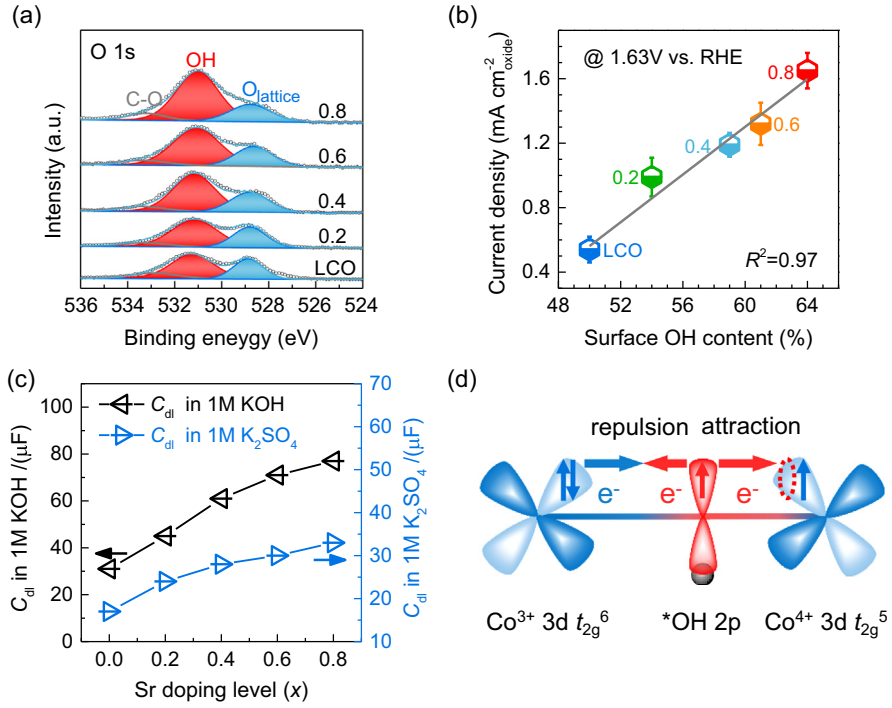

Fig 9. (a) XPS O 1 s spectra of LSCO-*x*. The spectra are fitted with three components including lattice oxygen ("$O_{lattice}$", light blue) at ~529 eV, surface adsorbed OH ("OH", red) at ~531 eV and surface carbonate ("C – O", gray) at ~533.5 eV, respectively; (b) OER current densities vs. the surface OH content derived from the fitting of O 1 s XPS spectra; (c) C_{dl} measured in 1 M KOH and 1 M K_2SO_4 as a function of ×, indicating the increase in OH^- adsorption; (d) schematic illustration for the interaction of electronic states in Co 3d-O 2p.

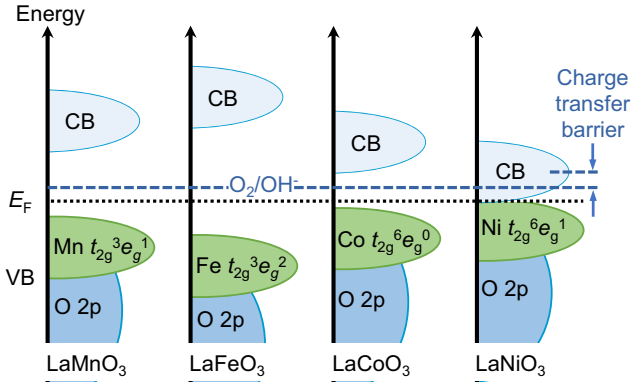

Fig 10. Schematics of energy band positions for first-row transition metal perovskite oxide ($LaMnO_3$, $LaFeO_3$, $LaCoO_3$ and $LaNiO_3$ respectively) [12,57,65], the energy difference between the CB and O_2/OH^- redox energy level is defined as the energy barrier for charge transfer associated with OER.

activities. The present study confirms that the hole state for promoting both surface oxygen intermediate adsorption and charge transfer is necessary for explaining the OER activities of perovskite oxide.

4. Conclusions

In this work, we investigated the electronic structure evolution of LSCO-*x* and its correlation with OER performance. Sr doping in LCO induces a transition from rhombohedral to cubic structure and shortens the Co – O bond length. Spectroscopic results show that LCO has low spin Co^{3+} with a $t_{2g}^6e_g^0$ configuration. Replacing La^{3+} with Sr^{2+} introduces Co^{4+} and doped hole states of empty t_{2g} character at the top of the valence band. The hole states lead to enhanced Co 3d-O 2p hybridization and a semiconductor-to-metal transition for × ≥ 0.2. Furthermore, XPS and electrochemical capacitance measurement results reveal that stronger Co 3d-O 2p hybridization improves the adsorption of oxygen intermediates on LSCO-*x* surface. As a result, metallic LSCO-0.8 was identified as the most active electrocatalyst. Our study highlights that hole states in the electronic structure of high valence TMO is the key for promoting OER performance.

Declaration of Competing Interest

The authors declare that they have no known competing financial interests or personal relationships that could have appeared to influence the work reported in this paper.

Acknowledgments

K.H.L. Zhang is grateful for funding support by the National Natural Science Foundation of China (Grant No. 21872116). J.C. gratefully acknowledges the financial support by the National Natural Science Foundation of China (Grant No. 21621091 and 21373166). Freddy E. Oropeza and Victor A. de la Peña O'Shea are grateful for the funding supported by the EU (ERC CoG HyMAP 648319) and Spanish AEI (NyMPhA PID2019-106315RB-I00). Victor A. de la Peña O'Shea also wishes to thank "Comunidad de Madrid" and European Structural Funds for their financial support to FotoArt-CM project (S2018/NMT-4367) and the Fundación Ramón Areces. C. M. Tian gratefully acknowledges financial support by the China Scholarship Council (CSC). K.H.L. Zhang and Jan P. Hofmann also ackonwledge the Sino-German Mobility Program (Grant No. M-0377). Preliminar spectroscopic measurements were performed at the CLAESS beamline at the ALBA synchrotron.

Appendix A. Supplementary data

Supplementary data to this article can be found online at https://doi.org/10.1016/j.jechem.2021.06.032.

References

[1] P.P. Edwards, V.L. Kuznetsov, W.I.F. David, N.P. Brandon, Energy Policy 36 (2008) 4356–4362.
[2] J. Mei, T. Liao, J. Liang, Y. Qiao, S.X. Dou, Z. Sun, Adv. Energy Mater. 10 (2020) 1901997.
[3] X. Wang, S. Qiu, J. Feng, Y. Tong, F. Zhou, Q. Li, L. Song, S. Chen, K.-H. Wu, P. Su, S. Ye, F. Hou, S.X. Dou, H.K. Liu, G.Q. Lu, C. Sun, J. Liu, J. Liang, Adv. Mater. 32 (2020) 2004382.
[4] T.R. Cook, D.K. Dogutan, S.Y. Reece, Y. Surendranath, T.S. Teets, D.G. Nocera, Chem. Rev. 110 (2010) 6474–6502.
[5] Y. Tong, H. Guo, D. Liu, X. Yan, P. Su, J. Liang, S. Zhou, J. Liu, G.Q. Lu, S.X. Dou, Angew. Chem. Int. Ed. 59 (2020) 7356–7361.
[6] D. Liu, Y. Tong, X. Yan, J. Liang, S.X. Dou, Batteries Supercaps 2 (2019) 743–765.
[7] I.C. Man, H.-Y. Su, F. Calle-Vallejo, H.A. Hansen, J.I. Martínez, N.G. Inoglu, J. Kitchin, T.F. Jaramillo, J.K. Nørskov, J. Rossmeisl, ChemCatChem 3 (2011) 1159–1165.
[8] M.T.M. Koper, J. Electroanal. Chem. 660 (2011) 254–260.
[9] L. Han, S. Dong, E. Wang, Adv. Mater. 28 (2016) 9266–9291.
[10] J. Song, C. Wei, Z.-F. Huang, C. Liu, L. Zeng, X. Wang, Z.J. Xu, Chem. Soc. Rev. 49 (2020) 2196–2214.
[11] J. Hwang, R.R. Rao, L. Giordano, Y. Katayama, Y. Yu, Y. Shao-Horn, Science 358 (2017) 751.
[12] Y. Wang, Y. Sui, J. Cheng, X. Wang, Z. Lu, W. Su, J. Phys. Chem. C 113 (2009) 12509–12516.
[13] H.B. Lu, G.Z. Yang, Z.H. Chen, S.Y. Dai, Y.L. Zhou, K.J. Jin, B.L. Cheng, M. He, L.F. Liu, H.Z. Guo, Y.Y. Fei, W.F. Xiang, L. Yan, Appl. Phys. Lett. 84 (2004) 5007–5009.
[14] Y. Zhao, Y. Hang, Y. Zhang, Z. Wang, Y. Yao, X. He, C. Zhang, D. Zhang, Electrochim. Acta 232 (2017) 296–302.
[15] A. Grimaud, A. Demortière, M. Saubanère, W. Dachraoui, M. Duchamp, M.-L. Doublet, J.-M. Tarascon, Nat. Energy 2 (2016) 16189.
[16] W.T. Hong, K.A. Stoerzinger, Y.-L. Lee, L. Giordano, A. Grimaud, A.M. Johnson, J. Hwang, E.J. Crumlin, W. Yang, Y. Shao-Horn, Energy Environ. Sci. 10 (2017) 2190–2200.
[17] J. Suntivich, K.J. May, H.A. Gasteiger, J.B. Goodenough, Y. Shao-Horn, Science 334 (2011) 1383–1385.
[18] S. Yagi, I. Yamada, H. Tsukasaki, A. Seno, M. Murakami, H. Fujii, H. Chen, N. Umezawa, H. Abe, N. Nishiyama, S. Mori, Nat. Commun. 6 (2015) 8249.
[19] A. Grimaud, K.J. May, C.E. Carlton, Y.-L. Lee, M. Risch, W.T. Hong, J. Zhou, Y. Shao-Horn, Nat. Commun. 4 (2013) 2439.
[20] A. Grimaud, O. Diaz-Morales, B. Han, W.T. Hong, Y.-L. Lee, L. Giordano, K.A. Stoerzinger, M.T.M. Koper, Y. Shao-Horn, Nat. Chem. 9 (2017) 457–465.
[21] G. Chen, W. Zhou, D. Guan, J. Sunarso, Y. Zhu, X. Hu, W. Zhang, Z.J.S.A. Shao, Sci. Adv. 3 (2017) e1603206.
[22] K.J. May, C.E. Carlton, K.A. Stoerzinger, M. Risch, J. Suntivich, Y.-L. Lee, A. Grimaud, Y. Shao-Horn, J. Phys. Chem. Lett. 3 (2012) 3264–3270.
[23] H. Wang, X. Chen, D. Huang, M. Zhou, D. Ding, H. Luo, ChemCatChem 12 (2020) 2768–2775.
[24] Z. Liu, Y. Sun, X. Wu, C. Hou, Z. Geng, J. Wu, K. Huang, L. Gao, S. Feng, CrystEngComm 21 (2019) 1534–1538.
[25] Y. Heo, S. Choi, J. Bak, H.-S. Kim, H.B. Bae, S.-Y. Chung, Adv. Energy Mater. 8 (2018) 1802481.
[26] Y. Liu, H. Dai, J. Deng, L. Zhang, Z. Zhao, X. Li, Y. Wang, S. Xie, H. Yang, G. Guo, Inorg. Chem. 52 (2013) 8665–8676.
[27] K.A. Stoerzinger, W.S. Choi, H. Jeen, H.N. Lee, Y. Shao-Horn, J. Phys. Chem. Lett. 6 (2015) 487–492.
[28] A. Guerrero, J. Bisquert, Curr. Opin. Electrochem. 2 (2017) 144–147.
[29] M.C. Alvarez-Galvan, V.A.D. O'Shea, G. Arzamendi, B. Pawelec, L.M. Gandia, J.L. G. Fierro, Appl. Catal. B: Environ. 92 (2009) 445–453.
[30] Y. Tong, Y. Guo, P. Chen, H. Liu, M. Zhang, L. Zhang, W. Yan, W. Chu, C. Wu, Y. Xie, Chem 3 (2017) 812–821.
[31] S. Zhou, X. Miao, X. Zhao, C. Ma, Y. Qiu, Z. Hu, J. Zhao, L. Shi, J. Zeng, Nat. Commun. 7 (2016) 11510.
[32] Y. Duan, S. Sun, S. Xi, X. Ren, Y. Zhou, G. Zhang, H. Yang, Y. Du, Z.J. Xu, Chem. Mater. 29 (2017) 10534–10541.
[33] A. Chainani, M. Mathew, D.D. Sarma, Phys. Rev. B 46 (1992) 9976–9983.
[34] G. Vankó, J.-P. Rueff, A. Mattila, Z. Németh, A. Shukla, Phys. Rev. B 73 (2006) 024424.
[35] X. Cheng, E. Fabbri, M. Nachtegaal, I.E. Castelli, M. El Kazzi, R. Haumont, N. Marzari, T.J. Schmidt, Chem. Mater. 27 (2015) 7662–7672.
[36] J.T. Mefford, X. Rong, A.M. Abakumov, W.G. Hardin, S. Dai, A.M. Kolpak, K.P. Johnston, K.J. Stevenson, Nat. Commun. 7 (2016) 11053.
[37] N.M.L.N.P. Closset, R.H.E. van Doorn, H. Kruidhof, J. Boeijsma, Powder Diffr. 11 (1996) 31–34.
[38] J. Ovenstone, J.S. White, S.T. Misture, J. Power Sources 181 (2008) 56–61.
[39] A. Nemudry, P. Rudolf, R. Schöllhorn, Chem. Mater. 8 (1996) 2232–2238.
[40] K.H.L. Zhang, Y. Du, A. Papadogianni, O. Bierwagen, S. Sallis, L.F.J. Piper, M.E. Bowden, V. Shutthanandan, P.V. Sushko, S.A. Chambers, Adv. Mater. 27 (2015) 5191–5195.
[41] C. Wei, Z.J. Xu, Small Methods 2 (2018) 1800168.
[42] S. Sun, H. Li, Z.J. Xu, Joule 2 (2018) 1024–1027.
[43] C. Wei, R.R. Rao, J. Peng, B. Huang, I.E.L. Stephens, M. Risch, Z.J. Xu, Y. Shao-Horn, Adv. Mater. 31 (2019) 1806296.
[44] T. Saitoh, T. Mizokawa, A. Fujimori, M. Abbate, Y. Takeda, M. Takano, Phys. Rev. B 56 (1997) 1290–1295.
[45] K.H.L. Zhang, Y. Du, P.V. Sushko, M.E. Bowden, V. Shutthanandan, S. Sallis, L.F.J. Piper, S.A. Chambers, Phys. Rev. B 91 (2015) 155129.
[46] H. Wadati, D. Kobayashi, H. Kumigashira, K. Okazaki, T. Mizokawa, A. Fujimori, K. Horiba, M. Oshima, N. Hamada, M. Lippmaa, M. Kawasaki, H. Koinuma, Phys. Rev. B 71 (2005) 035108.
[47] M.L. Baker, M.W. Mara, J.J. Yan, K.O. Hodgson, B. Hedman, E.I. Solomon, Coord. Chem. Rev. 345 (2017) 182–208.
[48] M.W. Haverkort, Z. Hu, J.C. Cezar, T. Burnus, H. Hartmann, M. Reuther, C. Zobel, T. Lorenz, A. Tanaka, N.B. Brookes, H.H. Hsieh, H.J. Lin, C.T. Chen, L.H. Tjeng, Phys. Rev. Lett. 97 (2006) 176405.
[49] Y. Kumagai, H. Ikeno, F. Oba, K. Matsunaga, I. Tanaka, Phys. Rev. B 77 (2008) 155124.
[50] L.A. Montoro, Electrochem. Solid-State Lett. 3 (1999) 410.
[51] L. Karvonen, M. Valkeapää, R.-S. Liu, J.-M. Chen, H. Yamauchi, M. Karppinen, Chem. Mater. 22 (2010) 70–76.
[52] Z. Hu, C. Grazioli, M. Knupfer, M.S. Golden, J. Fink, P. Mahadevan, A. Kumar, S. Ray, D.D. Sarma, S.A. Warda, D. Reinen, S. Kawasaki, M. Takano, C. Schüssler-Langeheine, C. Mazumdar, G. Kaindl, J. Alloys Compd. 343 (2002) 5–13.
[53] M. Merz P. Nagel C. Pinta A. Samartsev H. v. Löhneysen, M. Wissinger, S. Uebe, A. Assmann, D. Fuchs, S. Schuppler, Phys. Rev. B 82 2010 174416
[54] D. Fuchs, M. Merz, P. Nagel, R. Schneider, S. Schuppler, H. von Löhneysen, Phys. Rev. Lett. 111 (2013) 257203.
[55] J. Suntivich, W.T. Hong, Y.-L. Lee, J.M. Rondinelli, W. Yang, J.B. Goodenough, B. Dabrowski, J.W. Freeland, Y. Shao-Horn, J. Phys. Chem. C 118 (2014) 1856–1863.
[56] N.-T. Suen, S.-F. Hung, Q. Quan, N. Zhang, Y.-J. Xu, H.M. Chen, Chem. Soc. Rev. 46 (2017) 337–365.
[57] Y.-L. Lee, M.J. Gadre, Y. Shao-Horn, D. Morgan, Phys. Chem. Chem. Phys. 17 (2015) 21643–21663.
[58] M. Retuerto, L. Pascual, F. Calle-Vallejo, P. Ferrer, D. Gianolio, A.G. Pereira, Á. García, J. Torrero, M.T. Fernández-Díaz, P. Bencok, M.A. Peña, J.L.G. Fierro, S. Rojas, Nat. Commun. 10 (2019) 2041.
[59] L.C. Seitz, C.F. Dickens, K. Nishio, Y. Hikita, J. Montoya, A. Doyle, C. Kirk, A. Vojvodic, H.Y. Hwang, J.K. Norskov, T.F. Jaramillo, Science 353 (2016) 1011–1014.
[60] G. Fu, X. Wen, S. Xi, Z. Chen, W. Li, J.-Y. Zhang, A. Tadich, R. Wu, D.-C. Qi, Y. Du, J. Cheng, K.H.L. Zhang, Chem. Mater. 31 (2019) 419–428.
[61] Z. Shen, Y. Zhuang, W. Li, X. Huang, F.E. Oropeza, E.J.M. Hensen, J.P. Hofmann, M. Cui, A. Tadich, D. Qi, J. Cheng, J. Li, K.H.L. Zhang, J. Mater. Chem. A 8 (2020) 4407–4415.
[62] K.A. Stoerzinger, X. Renshaw Wang, J. Hwang, R.R. Rao, W.T. Hong, C.M. Rouleau, D. Lee, Y. Yu, E.J. Crumlin, Y. Shao-Horn, Top. Catal. 61 (2018) 2161–2174.
[63] K.A. Stoerzinger, W.T. Hong, E.J. Crumlin, H. Bluhm, Y. Shao-Horn, Acc. Chem. Res. 48 (2015) 2976–2983.
[64] K.A. Stoerzinger, L. Wang, Y. Ye, M. Bowden, E.J. Crumlin, Y. Du, S.A. Chambers, J. Mater. Chem. A 6 (2018) 22170–22178.
[65] C.C.L. McCrory, S. Jung, J.C. Peters, T.F. Jaramillo, J. Am. Chem. Soc. 135 (2013) 16977–16987.
[66] S. Trasatti, O.A. Petrii, J. Electroanal. Chem. 63 (1991) 711–734.
[67] J.D. Benck, Z. Chen, L.Y. Kuritzky, A.J. Forman, T.F. Jaramillo, ACS Catal. 2 (2012) 1916–1923.
[68] X. Li, H. Wang, Z. Cui, Y. Li, S. Xin, J. Zhou, Y. Long, C. Jin, J.B. Goodenough, Sci. Adv. 5 (2019) eaav6262.
[69] T. Saitoh, A.E. Bocquet, T. Mizokawa, H. Namatame, A. Fujimori, M. Abbate, Y. Takeda, M. Takano, Jpn. J. Appl. Phys. 32 (1993) 258.
[70] I. Yamada, A. Takamatsu, K. Asai, T. Shirakawa, H. Ohzuku, A. Seno, T. Uchimura, H. Fujii, S. Kawaguchi, K. Wada, H. Ikeno, S. Yagi, J. Phys. Chem. C 122 (2018) 27885–27892.